Journal of Solid State Chemistry 182 (2009) 2135–2140

Contents lists available at ScienceDirect

Journal of Solid State Chemistry

journal homepage: www.elsevier.com/locate/jssc

Synthesis of magnetic nickel spinel ferrite nanospheres by a reverse emulsion-assisted hydrothermal process

Jilin Zhang, Jianxin Shi *, Menglian Gong

Key Laboratory of Bioinorganic and Synthetic Chemistry of Ministry of Education, State Key Laboratory of Optoelectronic Materials and Technologies, School of Chemistry and Chemical Engineering, Sun Yat-Sen University, Guangzhou 510275, China

ARTICLE INFO

Article history:
Received 2 October 2008
Received in revised form
25 April 2009
Accepted 27 May 2009
Available online 2 June 2009

Keywords:
$NiFe_2O_4$
Nanospheres
Magnetic
Reverse emulsion
Hydrothermal

ABSTRACT

Nickel ferrite nanospheres were successfully synthesized by a reverse emulsion-assisted hydrothermal method. The reverse emulsion was composed of water, cetyltrimethyl ammonium bromide, polyoxyethylene(10)nonyl phenyl ether, iso-amyl alcohol and hexane. During the hydrothermal process, β-FeO(OH) and $Ni_{0.75}Fe_{0.25}(CO_3)_{0.125}(OH)_2 \cdot 0.38H_2O$ (INCHH) nanorods formed first and then transformed into nickel spinel ferrite nanospheres. The phase transformation mechanism is proposed based on the results of X-ray powder diffraction, transmission electron microscopy and energy-dispersive X-ray spectroscopy, etc. Nickel ferrite may form at the end of the INCHH nanorods or from the solution accompanied by the dissolution of β-FeO(OH) and INCHH nanorods. The X-ray photoelectron spectroscopy analysis shows that a few Fe^{3+} ions have been reduced to Fe^{2+} ions during the formation of nickel ferrite. The maximum magnetization of the nickel ferrite nanospheres obtained after hydrothermal reaction for 30 h is 55.01 emu/g, which is close to that of bulk $NiFe_2O_4$.

1. Introduction

Nanostructured magnetic materials have been attracting extensive attention because of their potential applications in catalysis, biotechnology, environment, magnetic fluids and magnetic resonance imaging (MRI) contrast agents, etc. [1–7].

As one of the magnetic nanomaterials, nickel ferrites have been intensively investigated for various applications such as gas-sensor, magnetic fluids, catalysts and magnetic materials, etc. [8–11]. The nickel ferrites have been synthesized by several methods. Monodisperse $NiFe_2O_4$ nanocrystals have been prepared by thermolysis [12] or by hydrolysis method [13]. Liu et al. have synthesized $NiFe_2O_4$ nanoparticles by the shock waves synthesis [14]. The room-temperature saturation magnetization (M_s) values of all the obtained-products are less than 40 emu/g, which are lower than that of the bulk one (55 emu/g). The superparamagnetic $NiFe_2O_4$ nanoparticles with diameters less than 10 nm have been synthesized by different methods like sonochemical decomposition process [15], reverse micelle technique [16] and aging treatment of the precipitated precursor at 145 °C [17]. The sol–gel method [18,19] and reverse microemulsion process [20] have been employed to prepare aggregate $NiFe_2O_4$ particles with the room-temperatue M_s values close to 55 emu/g. Wang has prepared highly crystalline $NiFe_2O_4$ nanoparticles with the room-temperature M_s slightly lower than that of the bulk one by the hydrothermal process at 140 °C for 12 h [21]. Zhou et al. have reported that the evolution and crystallization of $NiFe_2O_4$ nanoparticles could be readily synthesized by appropriately adjusting the processing factors under the hydrothermal process [22].

Among those methods, the hydrothermal reaction shows some advantages in controlling particle size, morphology and other characteristics by changing reaction time, temperature, pH value and other factors. In the hydrothermal process, the increased temperature and pressure will increase the solubility of most ionic species and the mobility of water which acts as a reactant. This allows Ostwald ripening to continue increasing the uniformity of the precipitates at a faster rate [23]. However, it is difficult to determine when Ostwald ripening finishes. So, the size of the as-prepared products always has two distribution regions [21,24]. On the other hand, the reverse emulsion method has been used to synthesize different kinds of nanoparticles. The size and its distribution of water pools in the reverse emulsion can be well controlled by adjusting the water/surfactant ratio, which will further control the size and morphology of the synthesized particles [23]. Therefore, it is easy to obtain nanoparticles like magnetite [25,26] and $CoFe_2O_4$ [27] with a narrow size distribution in the reverse emulsion system.

To utilize the advantages of both hydrothermal and reverse emulsion methods, a reverse emulsion-assisted hydrothermal process is used to synthesize nickel spinel ferrites with only one

Abbreviations: INCHH, $Ni_{0.75}Fe_{0.25}(CO_3)_{0.125}(OH)_2 \cdot 0.38H_2O$

* Corresponding author. Fax: +86 20 8411 2245.
E-mail address: chemshijx@163.com (J. Shi).

0022-4596/$ - see front matter Crown Copyright © 2009 Published by Elsevier Inc. All rights reserved.
doi:10.1016/j.jssc.2009.05.032

size distribution in the present work. The reverse emulsion was composed of water, cetyltrimethyl ammonium bromide (CTAB), polyoxyethylene(10)nonyl phenyl ether (NP10), iso-amyl alcohol and hexane. Nickel ferrite nanospheres were obtained and the formation mechanism of the nanospheres was proposed.

2. Experimental section

2.1. Preparation

All of chemical reagents used in the experiments were of analytical grade, except that NP10 was chemical grade. In a typical synthesis, 4.0 mL of NP10, 7.0 mL of 0.2 mol/L $Ni(NO_3)_2$ aqueous solution, 14.0 mL of 0.2 mol/L $Fe(NO_3)_3$ aqueous solution and 35.0 mL of hexane were mixed under stirring and then 2.80 g CTAB was dissolved in the above emulsion with the addition of 7.0 mL iso-amyl alcohol and finally, a transparent reverse emulsion was formed by dissolving 2.10 g of urea under stirring. 11.0 mL of the resulting emulsion was transferred into a 16 mL teflon-lined stainless autoclave, sealed and placed in an oven. The oven was heated from room temperature to 120 °C in about half an hour and maintained at this temperature for 2–30 h. Then the autoclave was cooled to room temperature naturally. The resulting product was washed with distilled water several times and dried at 90 °C in air.

2.2. Measurements

The X-ray powder diffraction (XRD) patterns of the samples were collected with a Rigaku D/max-2200 X-ray diffractometer using Cu$K\alpha$ radiation ($\lambda = 1.5406$ Å). The operation voltage and current were maintained at 40 kV and 30 mA, respectively. The IR spectra were measured on a Nicolet 330 FT-IR spectrometer, using pressed KBr tablets. The inductively coupled plasma-atomic emission spectrometry (ICP) analysis was carried out with a TJA IRIS (HR) instrument. The samples were dissolved in nitrohydrochloric acid before the ICP analysis. The X-ray photoelectron spectroscopy (XPS) measurements were carried out with a VG Scientific ESCALAB 250 system and Al$K\alpha$ ($h\nu = 1486.6$ eV) as the X-ray source. Transmission electron microscopic (TEM) images and high-resolution transmission electron microscopic (HRTEM) images were performed on a JEOL JEM-2010HR instrument with a working voltage of 200 kV. Energy-dispersive X-ray spectroscopy (EDS) was obtained with the instrument attached to the JEOL JEM-2010HR. The magnetic properties of the samples were measured with a Quantum Design MPMS XL-7 SQUID magnetometer.

3. Results and discussions

The yields of the samples obtained with the reverse emulsion-assisted hydrothermal process were more than 85%. The phase and purity of the samples were determined from the XRD measurements. The XRD patterns of the samples prepared by hydrothermal treatment at 120 °C for 2–30 h are shown in Fig. 1. The six samples obtained after reacting for 2–30 h are marked as "sample a" to "sample f" in alphabetical order, respectively. It can be seen that the phase of the samples changed as the holding time prolonged. The main phases for sample a can be indexed to $Ni_{0.75}Fe_{0.25}(CO_3)_{0.125}(OH)_2 \cdot 0.38H_2O$ (JCPDS No. 40-0215, iron nickel carbonate hydroxide hydrate, INCHH) and β-FeO(OH) (JCPDS No. 34-1266). As the holding time increases, the relative intensity of the peaks for these two phases decreases and finally the peaks disappear, while the peaks of $NiFe_2O_4$ (JCPDS No. 10-0325) appear gradually and become the single phase when the holding time is 24 h (Fig. 1e) or 30 h (Fig. 1f).

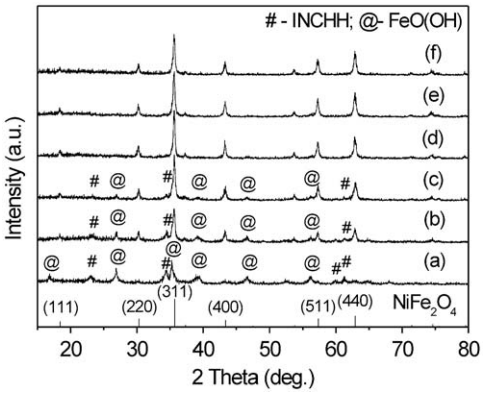

Fig. 1. X-ray diffraction patterns of the samples obtained by the reverse emulsion-assisted hydrothermal method for different time at 120 °C: (a) 2 h, (b) 6 h, (c) 12 h, (d) 18 h, (e) 24 h and (f) 30 h.

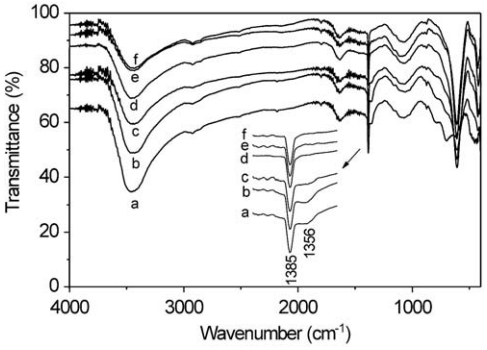

Fig. 2. IR analysis of the samples obtained by the reverse emulsion-assisted hydrothermal method for different time at 120 °C: (a) 2 h, (b) 6 h, (c) 12 h, (d) 18 h, (e) 24 h, (f) 30 h, The insert: IR spectra in the reign of 1300–1450 cm^{-1}.

The IR spectra of all the six samples are shown in Fig. 2. We can see that, the peak at ~1356 cm^{-1}, which belongs to the stretching vibration of CO_3^{2-}, exists in the spectra of samples a, b and c, while does not exist in the other three spectra. The results are consistent with those of the XRD analysis. The peak at ~1385 cm^{-1} shows that the O–H group exists in all the samples, which originates from FeOOH (samples a, b and c) or from the absorption of water and OH^- on the surface of $NiFe_2O_4$ spheres (samples d, e and f).

The ICP analysis results show that the molar ratio of Ni/Fe for the sample f is 0.85/2.15. Compared with the formula $NiFe_2O_4$, there is a lack of nickel or a superabundance of iron. Combined with the XRD results, we assume that the chemical formula for sample f can be described as $Ni_{0.85}Fe_{2.15}O_4$. Considering the charge balance, a few Fe^{3+} ions may have been reduced to Fe^{2+}.

To approve this assumption, XPS analysis was used to find out whether there were Fe^{2+} ions in the sample f. Since the core-hole lifetime in photoemission process (10^{-5} s) is much faster than the hopping frequency, the Fe^{3+} and Fe^{2+} ions in octahedral sites are distinguishable in XPS [28].

In case of $NiFe_2O_4$ with only trivalent Fe ions [29], the Fe $2p_{3/2}$ region of the XPS spectrum can be divided into two peaks at the binding energy of 710.39 and 712.92 eV, which indicates that the Fe^{3+} species exist in more than one chemical state. These two chemical states may be related to different coordination environments of the Fe^{3+} in spinel structure, the tetrahedral and the octahedral environment: Fe^{3+}_{tet} at the higher binding energy and Fe^{3+}_{oct} at the lower binding energy. Specially, there is a shake-up

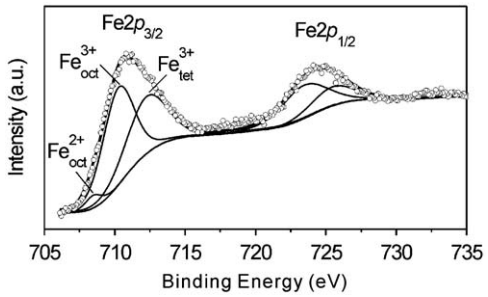

Fig. 3. The XPS spectrum of Fe 2*p* for sample f. The experimental data: circles and the fitted curves: solid lines.

satellite structure for tetrahedral or octahedral Fe^{3+} at around 718.9 eV. The XPS spectrum of Fe $2p_{3/2}$ in γ-Fe_2O_3 [28] is similar.

While in Fe_3O_4 [28,30], the satellite structures between 714 and 720 eV are smeared out. This is mainly due to the overlap of the peaks from the tetrahedral Fe^{3+}, octahedral Fe^{3+} and octahedral Fe^{2+} components with different intensity at the same binding energy. The key point is the existence of Fe^{2+} component, whose Fe $2p_{3/2}$ appears at the binding energy of 708.45 eV with a shake-up satellite structure at 715.16 eV.

Fig. 3 is the XPS spectrum of Fe 2*p* for sample f. There is no obvious peak between 714 and 720 eV. So there are Fe^{2+} ions in the nickel ferrite (sample f). The spectrum was fitted with three-components using the XPSPEAK41 program and Shirley-type background (Fig. 3). The binding energy values for $2p_{3/2}$ of tetrahedral and octahedral Fe^{3+} are found to be 712.70 and 710.51 eV, respectively, which are close to the results in Ref. [29], while the value for $2p_{3/2}$ of octahedral Fe^{2+} is 708.45 eV. Fig. 3 shows that the fitted overall curve is in good accordance with the experimental data.

In spinel ferrites, the molar ratio of the octahedral and tetrahedral sites of the oxygen lattice is 2:1 and Ni^{2+} and Fe^{2+} ions prefer to occupy the octahedral sites [31]. Combined with the results of XRD, ICP and XPS, the chemical formula of $Ni_{0.85}Fe_{2.15}O_4$ for sample f could be written as $[Fe^{3+}]_{tet}[Ni^{2+}_{0.85}Fe^{2+}_{0.15}Fe^{3+}]_{oct}O_4$. Because the radii of Ni^{2+} and Fe^{2+} ions are very close, the replacement of Ni^{2+} by Fe^{2+} will not change the lattice structure of nickel spinel ferrite.

The TEM images of the samples obtained with the reverse emulsion-assisted hydrothermal method at 120 °C for different time are shown in Fig. 4. Fig. 4a shows that the product prepared at 120 °C for 2 h is mainly nanorods with length of 100–200 nm and diameters of about 10 nm. Fig. 4b shows that nanospheres with diameters of 75–125 nm appear when the holding time was prolonged to 6 h, while the nanorods with diameters of 70–150 nm are still the dominative morphology. The nanospheres become the main morphology when the holding time was 12 h and the diameters increase to 100–150 nm (Fig. 4c). The diameters increase to 95–190 nm when the holding time was 18 h (Fig. 4d), while the diameters of sample e are 70–185 nm (Fig. 4e). With further increasing the time to 30 h, all the products are nanospheres with the diameters of 60–160 nm (Fig. 4f). The decrease of sphere diameter with prolonging reaction time was mainly due to the improvement of crystallinity, when the condensing of assembled nanoparticles occurred. The insert of Fig. 4f shows that the nanospheres in sample f with only one size distribution have been obtained with the reverse emulsion-assisted hydrothermal process.

Fig. 5 is the HRTEM images and the corresponding EDS patterns of the nanorods and the nanospheres mentioned above. The lattice plane spacing of the nanorod in Fig. 5a (sample c) is 0.743 nm which is close to the (110) spacing of β-FeO(OH). The EDS analysis (Fig. 5d) for these nanorods shows that no Ni atom is detected, which indicates that there are β-FeO(OH) nanorods in sample c. The Cu peaks come from the copper grids for the TEM measurement. The lattice plane spacing of the nanorod in Fig. 5b (sample c) is 0.586 nm which is lower than the (003) spacing of INCHH (0.775 nm). And the Fe/Ni ratio of the nanorod is 1 (Fig. 5e), with more Fe ions compared to that of INCHH. It may be due to the occurrence of phase transformation from INCHH to nickel spinel ferrite, where H_2O and CO_2 are lost and the bonding changes. While the lattice plane spacing of the sphere is 0.483 nm which is the typical (111) spacing of $NiFe_2O_4$ structures (Fig. 5c, sample e). The Fe/Ni ratio of the sphere obtained from the EDS analysis is close to 2 (Fig. 5f). Combined with the XRD results, we can conclude that the nanorods formed at the first period of hydrothermal reaction are composed of β-FeO(OH) and INCHH and with the increase of the reaction time, they gradually transformed into nickel ferrites with spherical morphology.

This transformation can be explained from kinetics and thermodynamics. The standard enthalpy of formation ($\Delta_f H^{1/2}_m$) of β-FeO(OH) is (-554.7 ± 1.9) kJ/mol [32] and that of $NiFe_2O_4$ is -1084.49 kJ/mol. The standard Gibbs' free energy of formation ($\Delta_f G^{1/2}_m$) for $NiFe_2O_4$ is -1122.04 kJ/mol, but we did not find the $\Delta_f G^{1/2}_m$ value for β-FeO(OH). The formation of β-FeO(OH) and $NiFe_2O_4$ take place in the solution and the contribution of the entropy change ($\Delta S^{1/2}_m$) to $\Delta_f G^{1/2}_m$ is small. Therefore, the values of $\Delta_f G^{1/2}_m$ for β-FeO(OH) and $NiFe_2O_4$ should keep the same sequence as that of $\Delta_f H^{1/2}_m$. The kinetically favored products, β-FeO(OH) and INCHH, form at the first period of hydrothermal reaction and the final one is the thermodynamically stable phase, $NiFe_2O_4$.

According to the results of XRD, TEM and EDS analyses, the formation mechanism of the nickel ferrite nanospheres in this system is described as Fig. 6.

In the reverse emulsion system, the surfactants CTAB and NP10 have the hydrophobic portion on the outside exposed to the non-polar solvent, hexane. As a result, a large number of spherical "water pools" form in hexane. Iso-amyl alcohol acts as cosurfactant to stabilize the system. The reactions are restricted in the water pools. Upon heating, urea is hydrolyzed to release NH_3 and CO_2 which are the sources of OH^- and CO_3^{2-} ions, respectively. β-FeO(OH) nanorods form first with the increase of pH value. Liang et al. [33] reported that acicular FeO(OH) formed within the pH value of 1.6–2.0 in a microemulsion system. Water may act as a reactant and accelerate the kinetics of the hydrolysis reactions in the hydrothermal system [23]. INCHH form with the increase of OH^- and CO_3^{2-} ions. The length of β-FeO(OH) and INCHH nanorods is restricted by the sizes of water pools. As the reaction time further increases, the nanorods will disappear and transform to $NiFe_2O_4$ spheres, with the diameters restricted too.

The spinel phase might form through two routes. The first one is that nickel ferrite forms at the end of the nanorods of INCHH with the release of H_2O and CO_2 molecules and the addition of Fe^{3+} from the solution as shown in the insert of Fig. 4a. The second one is that β-FeO(OH) and a part of INCHH dissolve in the solution and then $NiFe_2O_4$ nuclei are formed from the solution when the concentration of the precursor species increases to a certain oversaturation (the insert of Fig. 4b). The dissolution of FeO(OH) and INCHH can also be demonstrated by the reduction of the length of nanorods as shown in Fig. 4. The nuclei become larger and the nanorods disappear gradually. The nanoparticles formed in the nanoreactor assemble to a spherical particle or even a single crystal with spherical shape. The single-crystalline can be confirmed by the electron diffraction pattern (insert of Fig. 4e). The transformation process of the morphology is similar to that of Fe_3O_4 hollow spheres prepared by the hydrothermal method [34].

To better understand the role of surfactants and reverse emulsion system in the synthesis of $NiFe_2O_4$, a hydrothermal

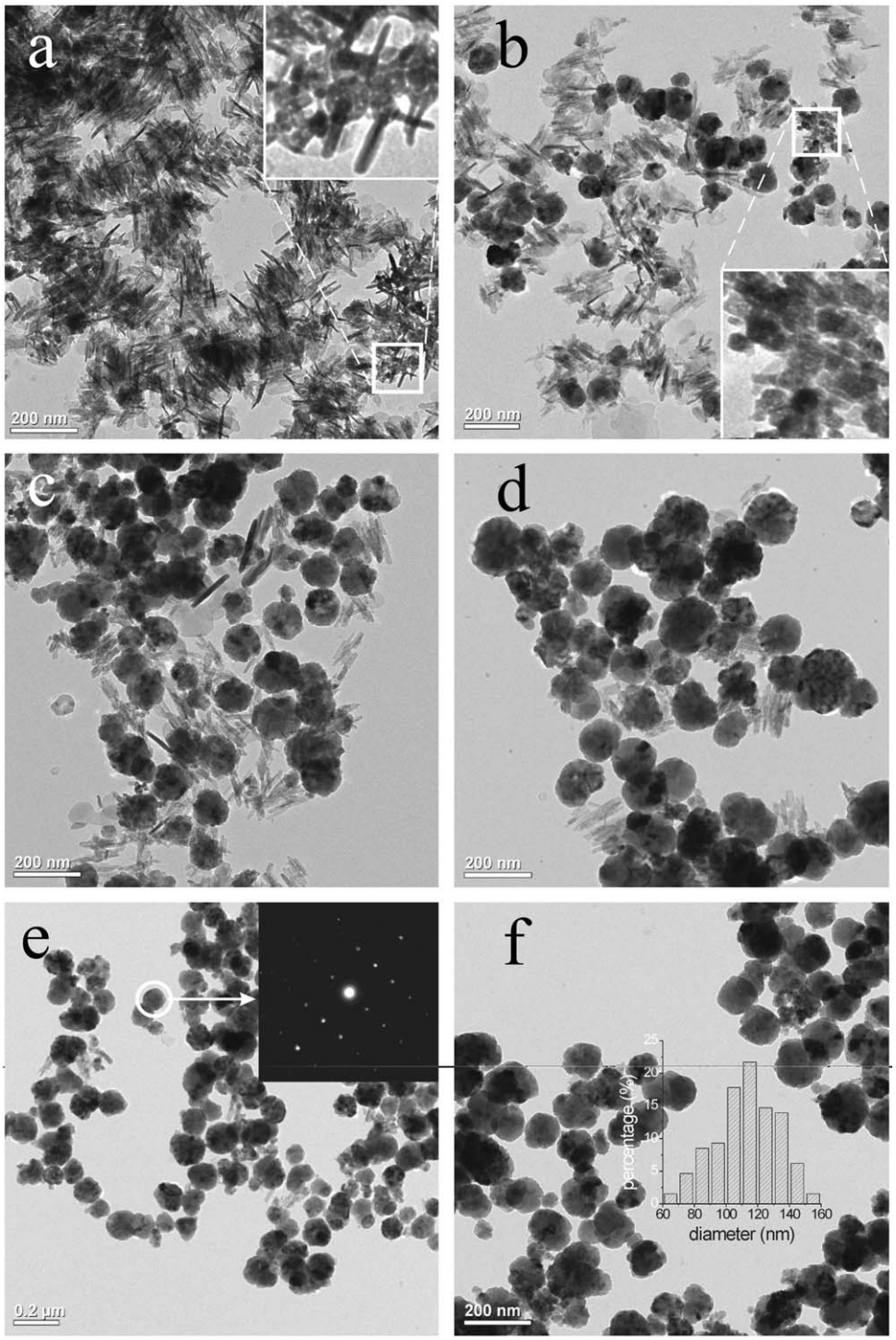

Fig. 4. TEM images of the samples hydrothermally treated for different time: (a) 2 h, the insert is 4 times as the square, showing nanospheres on the end of nanorods, (b) 6 h, the insert is 4 times as the square, showing the nuclei, (c) 12 h, (d) 18 h, (e) 24 h, the insert is the electron diffraction pattern of the entire sphere in the circle and (f) 30 h, the insert is a histogram of the size distribution for sample f.

process without surfactants was also carried out. The XRD patterns (not shown) indicate that the products obtained in this case are the kinetically favored, β-FeO(OH) and INCHH, while the $NiFe_2O_4$ phase can not form even when the reaction time lasted for 30 h.

Therefore, the function of CTAB and NP10 is not only to help forming nano- or micro-reactors to restrict the space of the reaction, but also to affect the thermodynamic state of $NiFe_2O_4$ solid nuclei by the formation of reverse emulsion. The former plays an important role in controlling the size and morphology of the synthesized particles, while the latter is a decisive factor to the nucleation growth in some cases and will result in the different products through the hydrothermal processes with surfactants or not. The reverse emulsion-assisted hydrothermal system could be applied to synthesize other spherical materials with similar structure by changing the reacting parameters.

The magnetic properties of the products obtained after reaction for 24 h (sample e) and 30 h (sample f) are shown in

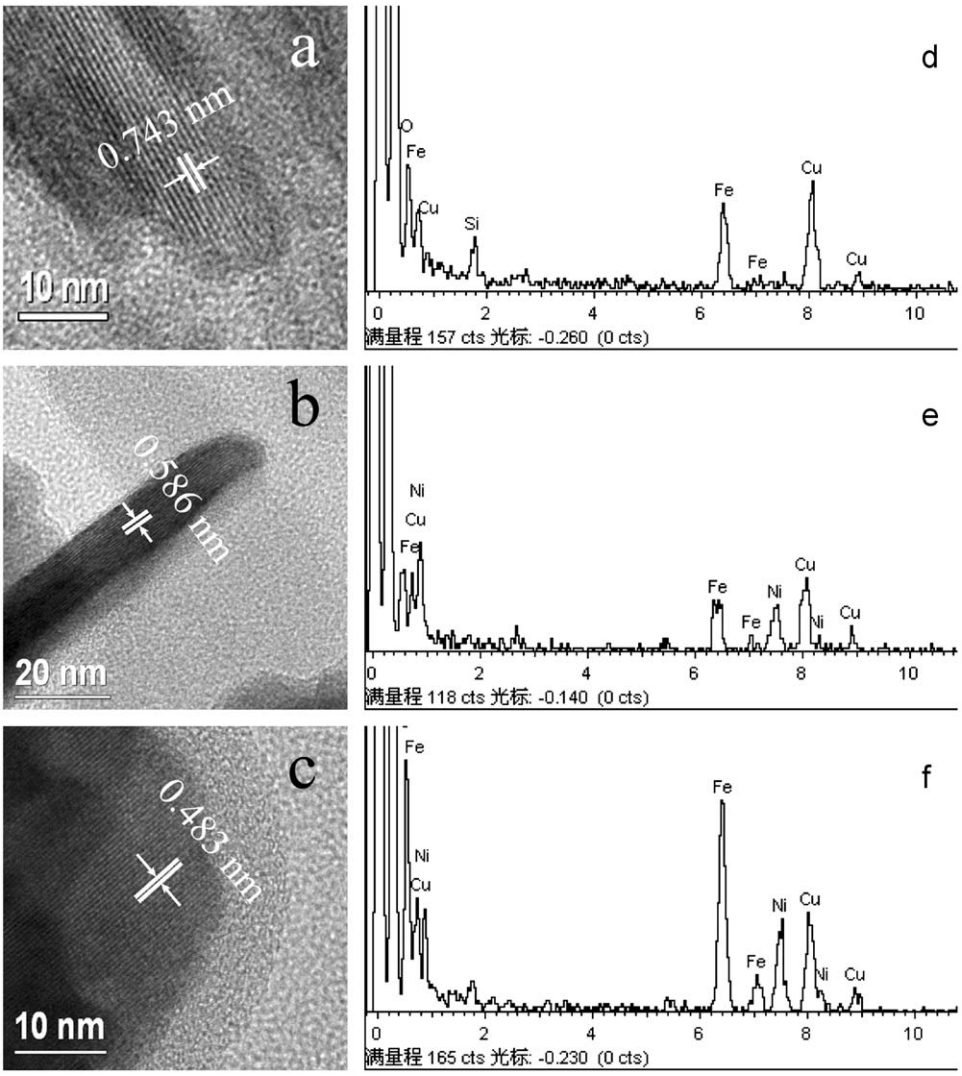

Fig. 5. HRTEM images of different morphologies and their corresponding EDS patterns: (a) light gray nanorods in sample c, (b) a dark nanorod in sample c, (c) a part of a nanosphere in sample e, (d) EDS pattern for (a), (e) EDS pattern for (b) and (f) EDS pattern for (c).

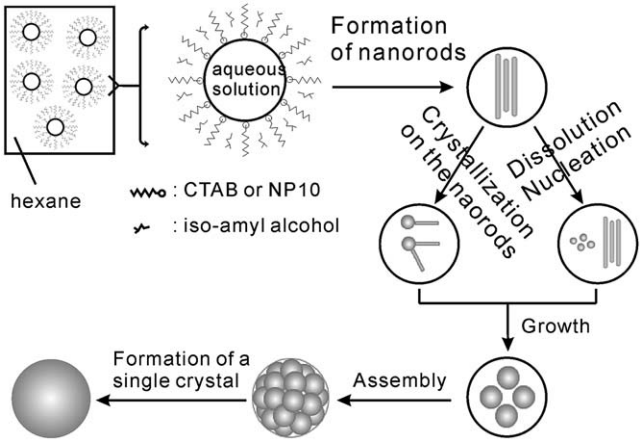

Fig. 6. Schematic illustration of the formation process of $NiFe_2O_4$ nanospheres. The scheme is simplified by omitting surfactants and cosurfactant.

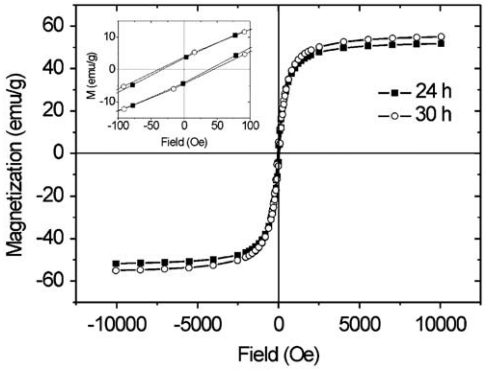

Fig. 7. Hysteresis curves of $NiFe_2O_4$ nanospheres hydrothermally treated at 24 and 30 h, measured at 293 K. The insert is a part of the hysteresis curves between −100 and 100 Oe.

Fig. 7. The hysteresis curves were collected at 293.0 K while the applied magnetic field changed between 10 and −10 kOe. Upon measuring, the magnetic field was first increased from 0 to 10 kOe (the magnetization data collected at this part are not given here). The maximum magnetization (M_{max}) at the applied field of 10 kOe increases with increasing reaction time, 51.78 emu/g for sample e and 55.01 emu/g for sample f, respectively. The M_{max} of sample f is close to the saturation magnetization of bulk $NiFe_2O_4$ (55 emu/g), which is mainly due to the substitution of a part of Ni^{2+} in the

octahedral sites by Fe^{2+} with a higher magnetic moment ($4.9\mu_B$). The coercivities of the samples increase with the prolonged reaction time, from 35.66 Oe for sample e to 41.77 Oe for sample f.

4. Conclusions

In summary, nickel ferrite nanospheres in one distribution region of 60–160 nm have been successfully prepared by a reverse emulsion-assisted hydrothermal process at low temperature. The two size distribution regions can be easily avoided in the hydrothermal system by the combination of emulsion. The morphology and size can be controlled by introducing a reverse emulsion system. A phase transformation can be achieved by changing the reaction time. The formation mechanism of nickel ferrite nanospheres has been speculated by the analyses of composition, morphology and valence of the samples. β-FeO(OH) and INCHH nanorods with restricted diameters form firstly in the water pools. Thereafter, nickel ferrite nanoparticles forms both from the solution and on the nanorods, accompanied by the dissolution of nanorods. The nanoparticles grow and assemble to a nanosphere within the separate water pool. The XPS analysis shows that a few Fe^{3+} ions have been reduced to Fe^{2+} ions during the formation of nickel ferrite. The maximum magnetization of the obtained spherical nickel ferrite is close to the saturation magnetization of the bulk $NiFe_2O_4$.

Acknowledgments

This work was financially supported by grants from the Guangdong Province Government (ZB2003A07), the Science and Technical Projects of Guangzhou (2005J1-C0241).

References

[1] T. Pellegrino, S. Kudera, T. Liedl, A.M. Javier, L. Manna, W.J. Parak, Small 1 (2005) 48–63.
[2] I. Safarik, M. Safarikova, Monatsh. Chem. 133 (2002) 737–759.
[3] M. Arruebo, R. Fernandez-Pacheco, M.R. Ibarra, J. Santamaria, Nano Today 2 (2007) 22–32.
[4] A.F. Ngomsik, A. Bee, M. Draye, G. Cote, V. Cabuil, Comptes Rendus Chimie. 8 (2005) 963–970.
[5] A.H. Lu, E.L. Salabas, F. Schuth, Angew. Chem. Int. Ed. 46 (2007) 1222–1244.
[6] A.R. Tao, S. Habas, P.D. Yang, Small 4 (2008) 310–325.
[7] U. Jeong, X.W. Teng, Y. Wang, H. Yang, Y.N. Xia, Adv. Mater. 19 (2007) 33–60.
[8] X.F. Chu, D.L. Jiang, C.M. Zheng, Sensor Actuat. B 123 (2007) 793–797.
[9] E. Hasmonay, J. Depeyrot, M.H. Sousa, F.A. Tourinho, J.C. Bacri, R. Perzynski, Y.L. Raikher, I. Rosenman, J. Appl. Phys. 88 (2000) 6628–6635.
[10] S. Rana, R.S. Srivastava, M.M. Sorensson, R.D.K. Misra, Mater. Sci. Eng. B 119 (2005) 144–151.
[11] Y.L. Raikher, V.I. Stepanov, J. Depeyrot, M.H. Sousa, F.A. Tourinho, E. Hasmonay, R. Perzynski, J. Appl. Phys. 96 (2004) 5226–5233.
[12] N.Z. Bao, L.M. Shen, Y.H. Wang, P. Padhan, A. Gupta, J. Am. Chem. Soc. 129 (2007) 12374–12375.
[13] S. Chkoundali, S. Ammar, N. Jouini, F. Fievet, P. Molinie, M. Danot, F. Villain, J.M. Greneche, J. Phys.: Condens. Matter 16 (2004) 4357–4372.
[14] J.J. Liu, H.L. He, X.G. Jin, Z.P. Hao, Z.Q. Hu, Mater. Res. Bull. 36 (2001) 2357–2363.
[15] K.V.P.M. Shafi, Y. Koltypin, A. Gedanken, R. Prozorov, J. Balogh, J. Lendvai, I. Felner, J. Phys. Chem. B 101 (1997) 6409–6414.
[16] A. Kale, S. Gubbala, R.D.K. Misra, J. Magn. Magn. Mater. 277 (2004) 350–358.
[17] J.H. Nam, W.K. Kim, S.J. Park, Phys. Status Solidi A 201 (2004) 1838–1841.
[18] S. Prasad, N.S. Gajbhiye, J. Alloys Compd. 265 (1998) 87–92.
[19] D.H. Chen, X.R. He, Mater. Res. Bull. 36 (2001) 1369–1377.
[20] J.Y. Fang, N. Shama, L.D. Tung, E.Y. Shin, C.J. O'Connor, K.L. Stokes, G. Caruntu, J.B. Wiley, L. Spinu, J.K. Tang, J. Appl. Phys. 93 (2003) 7483–7485.
[21] J. Wang, Mat. Sci. Eng. B 127 (1) (2006) 81–84.
[22] J. Zhou, J.F. Ma, C. Sun, L.J. Xie, Z.Q. Zhao, H. Tian, Y.G. Wang, J.T. Tao, X.Y. Zhu, J. Am. Ceram. Soc. 88 (2005) 3535–3537.
[23] M.A. Willard, L.K. Kurihara, E.E. Carpenter, S. Calvin, V.G. Harris, Int. Mater. Rev. 49 (2004) 125–170.
[24] D.H. Chen, D.R. Chen, X.L. Jiao, Y.T. Zhao, M.S. He, Powder Technol. 133 (2003) 247–250.
[25] Y. Lee, J. Lee, C.J. Bae, J.G. Park, H.J. Noh, J.H. Park, T. Hyeon, Adv. Funct. Mater. 15 (2005) 503–509.
[26] J. Baier, J. Koetz, S. Kosmella, B. Tiersch, H. Rehage, J. Phys. Chem. B 111 (2007) 8612–8618.
[27] A.J. Rondinone, A.C.S. Samia, Z.J. Zhang, J. Phys. Chem. B 103 (1999) 6876–6880.
[28] T. Fujii, F.M.F. de Groot, G.A. Sawatzky, F.C. Voogt, T. Hibma, K. Okada, Phys. Rev. B 59 (1999) 3195–3202.
[29] F. Li, X.F. Liu, Q.Z. Yang, J.J. Liu, D.G. Evans, X. Duan, Mater. Res. Bull. 40 (2005) 1244–1255.
[30] I. Banerjee, Y.B. Khollam, C. Balasubramanian, R. Pasricha, P.P. Bakare, K.R. Patil, A.K. Das, S.V. Bhoraskar, Scr. Mater. 54 (2006) 1235–1240.
[31] S. Smit, H.P.J. Wijn, in: P.T. Library, N.V. Philips (Eds.), Ferrites, Wiley, New York, 1959.
[32] L. Mazeina, S. Deore, A. Navrotsky, Chem. Mater. 18 (2006) 1830–1838.
[33] X.J. Liang, Y.X. Yang, X.N. Liu, H. Zhu, H.P. Ying, Z.Y. Zhou, Y.R. Chen, Russ. J. Inorg. Chem. 53 (2008) 367–371.
[34] L.P. Zhu, H.M. Xiao, W.D. Zhang, G. Yang, S.Y. Fu, Cryst. Growth Des. 8 (2008) 957–963.